



Unveiling the interplay between light-driven CO₂ photocatalytic reduction and carbonaceous residues decomposition: A case study of Bi₂WO₆-TiO₂ binanosheets



Lan Yuan^{a,b}, Kang-Qiang Lu^{a,b}, Fan Zhang^b, Xianzhi Fu^{a,b}, Yi-Jun Xu^{a,b,*}

^a State Key Laboratory of Photocatalysis on Energy and Environment, College of Chemistry, Fuzhou University, Fuzhou, 350116, PR China

^b College of Chemistry, New Campus, Fuzhou University, Fuzhou, 350116, PR China

ARTICLE INFO

Keywords:

Light-driven
CO₂ photoreduction
Carbonaceous residues decomposition
Bi₂WO₆-TiO₂ binanosheets

ABSTRACT

One critical issue to which special attention should be paid during the activity evaluation of photocatalytic CO₂ reduction is the possible carbonaceous residues on the photocatalyst, which may decompose into CO/CH₄, causing overestimation of the activity. In this regard, a contrast test under N₂ atmosphere instead of CO₂ has been widely employed as one cost-effective approach to confirm whether carbonaceous residues contribute to the carbon-containing products formation. However, this method might otherwise result in underestimation of the activity, according to the case study of as-fabricated Bi₂WO₆-TiO₂ binanosheets (B-T) in this work. Based on integrative studies of B-T sample under N₂ and CO₂ atmosphere, we for the first time unveil the co-existence of a competition and an interaction relationship between light-driven carbonaceous residues decomposition and photocatalytic CO₂ reduction, which further emphasizes the necessity of removing organic residues from photocatalysts and carefully analysing the origin of carbon-containing products to estimate the photocatalytic performance towards CO₂ reduction in a more accurate way. Moreover, this work could provide some enlightenment on designing and/or synthesising more efficient photocatalysts for CO₂ reduction with high selectivity for CH₄ formation, where rational construction of Z-scheme heterostructures is highlighted.

1. Introduction

The expected depletion of fossil fuel reserves and environmental concerns associated with increasing atmospheric CO₂ emission are posing great danger for our ecology and living environment on the earth [1,2]. It is an urgent task to attempt to reduce our dependency on fossil fuels and meanwhile release the environmental burden, which have recently boosted tremendous research activities on CO₂ capture, storage and utilization [3–6]. Among various available strategies, artificial photosynthesis that inspired by natural photosynthesis in green plants, using inexhaustible solar energy to convert CO₂ and H₂O into carbon-containing solar fuels provides a package solution to current energy demands and environmental issues [7–10]. Despite tremendous progresses that have been made in the field of photocatalytic CO₂ reduction [11–17], it is still of great significance to gain more fundamental understanding of this reaction, which would help us toward designing more efficient photocatalysts with improved activity and selectivity for CO₂ photoreduction.

Thereinto, one critical issue to which special attention should be paid during the research of photocatalytic CO₂ reduction is the possible

carbonaceous residues on the photocatalyst [18–21]. Previous studies have suggested that organic substances including solvents, reactants, and surfactants involved in the catalyst preparation may leave carbonaceous residues in the final product, which may decompose into small molecules such as CO and CH₄ during photocatalysis, causing overestimation of the catalytic activity [20,21]. In this regard, isotopic ¹³CO₂ labeling experiments are mostly suggested to help confirm that the carbon-containing products are derived from CO₂ rather than from carbonaceous impurities [18,19,21]. In addition, a contrast test of activity in an inert gas environment (N₂ or Ar) instead of CO₂ under identical conditions has also been widely employed as one cost-effective approach to confirm whether the carbonaceous residues on photocatalysts contribute to the carbon-containing products formation [18,19,21].

However, we herein propose that the method of contrast test under N₂ atmosphere might otherwise result in underestimation of the activity, based on the case study of as-fabricated Bi₂WO₆-TiO₂ binanosheets (B-T). Design and preparation of the B-T material are encouraged by the reasons that: TiO₂ is a representative semiconductor in the study of CO₂ photoreduction [22–28], and its activity is often

* Corresponding author.

E-mail address: yjxu@fzu.edu.cn (Y.-J. Xu).

restricted by the serious unwanted electron-hole pairs recombination [29–33]; Bi_2WO_6 possessing good stability and matchable energy band with TiO_2 is of great potential to couple with TiO_2 to enhance the charge-carrier transfer through heterostructure assembly [34–41]. In detail, the B-T sample was fabricated through an electrostatic self-assembly approach between positively charged A-TNS, i.e., TiO_2 nanosheets functionalized by 3-aminopropyl-triethoxysilane (APTES), and negatively charged Bi_2WO_6 nanosheets (BWO).

Through integrative study of B-T sample under N_2 and CO_2 atmosphere, we for the first time unveil the interplay, i.e., co-existence of a competition and an interaction relationship between the light-driven carbonaceous residues decomposition and photocatalytic CO_2 reduction. On one hand, large amount of CO and CH_4 were detected from the reaction system under N_2 , which is verified to come from carbonaceous residues decomposition that mainly originated from the employed APTES for the modification of TNS; however, once N_2 was replaced with CO_2 , the detected amount of CO/ CH_4 would significantly be decreased. On the other hand, reaction-time-lengthening evaluation under N_2 atmosphere in combination with controlled experiments show that the released CO from the carbonaceous residues decomposition can be further reduced to CH_4 with the participation of H_2O , which is one of the key reaction steps in photocatalytic CO_2 reduction. These results further emphasize the necessity of removing organic residues from photocatalysts and carefully analysing the origin of the carbon-containing products for estimating the performance towards photocatalytic CO_2 reduction. In addition, in-depth mechanism investigations indicate that the addition of BWO into A-TNS boosts the transformation of CO to CH_4 due to the enhanced H_2O oxidation, benefiting from the efficient Z-scheme charge transfer within B-T composite. This work would be expected to provide some enlightenment on designing and/or synthesising more efficient photocatalysts for CO_2 reduction with high selectivity for CH_4 formation, where the Z-scheme heterostructure assembly can be adopted in a rational manner.

2. Experimental section

2.1. Materials

Cetyltrimethyl ammonium bromide (CTAB) was supplied by Sigma-Aldrich. Tetraethyl titanate ($\text{Ti}(\text{OBu})_4$, 98%), hydrofluoric acid (47%), sodium tungstate dihydrate ($\text{Na}_2\text{WO}_4 \cdot 2\text{H}_2\text{O}$), bismuth nitrate pentahydrate ($\text{Bi}(\text{NO}_3)_3 \cdot 5\text{H}_2\text{O}$), 3-aminopropyl-triethoxysilane ($\text{C}_9\text{H}_{23}\text{NO}_3\text{Si}$, APTES), ethanol ($\text{C}_2\text{H}_5\text{OH}$), were obtained from Sinopharm Chemical Reagent Co., Ltd. (Shanghai, China). All materials were used as received without further purification. Deionized (DI) water used in the synthesis process was obtained from local sources.

2.2. Preparation and functionalization of TiO_2 nanosheets (TNS)

Anatase TiO_2 nanosheets (denoted as TNS) were synthesized according to our previously reported method [42,43]. Typically, 5 ml of $\text{Ti}(\text{OBu})_4$ and 1 ml of hydrofluoric acid solution were mixed in a dried Teflon autoclave with a capacity of 50 ml, and then kept at 453 K for 24 h. *Caution! Hydrofluoric acid is extremely corrosive and toxic, and should be handled with extreme care.* After being cooled to room temperature, the white powder was separated by centrifugation and washed with ethanol and DI water for several times. To functionalize the surface of TNS with positive charge, 0.4 g of the as-obtained TNS was first dispersed in 200 ml of ethanol by sonication for 30 min, followed by addition of 2 ml of APTES. Then, the mixture was kept at 333 K for 4 h with stirring. Afterwards, APTES functionalized TNS (A-TNS) were sufficiently rinsed with ethanol to remove the remaining APTES moiety and then dried at 333 K in an electronic oven for further use.

2.3. Preparation of Bi_2WO_6 nanosheets (BWO)

Bi_2WO_6 nanosheets (denoted as BWO) were synthesized by the reported method [44]. Typically, 1 mmol $\text{Na}_2\text{WO}_4 \cdot 2\text{H}_2\text{O}$, and 2 mmol $\text{Bi}(\text{NO}_3)_3 \cdot 5\text{H}_2\text{O}$ and 0.05 g CTAB were added in 80 ml deionized water. After 30 min stirring, the mixed solution was poured into a 100 ml Teflon-lined autoclave. Then the autoclave was sealed into a stainless steel tank and treated at 393 K for 24 h. After being cooled to room temperature, the product was collected and washed several times with DI water and dried at 333 K in air for 10 h.

2.4. Fabrication of $\text{Bi}_2\text{WO}_6\text{-TiO}_2$ binanosheets (B-T)

$\text{Bi}_2\text{WO}_6\text{-TiO}_2$ binanosheets (denoted as B-T) were prepared using an electrostatic self-assembly method. Typically, BWO aqueous suspension (0.5 mg ml⁻¹) was added dropwise into A-TNS aqueous solution (1 mg ml⁻¹) using a pipette under vigorous magnetic stirring. After being kept stirring at room temperature for 1 h, the B-T photocatalysts were isolated by filtration, washed with DI water and dried in an oven overnight at 333 K. The weight ratio of BWO in the B-T composite was 10%. For comparison, the sample of physically mixed A-TNS and BWO was prepared by mixing them with a mortar keeping the weight addition ratio of BWO as 10%.

2.5. Characterization

Zeta potentials (ζ) measurements of the samples were determined by dynamic light scattering analysis (Zeta sizer 3000HSA) at room temperature. The X-ray diffraction (XRD) patterns of the samples were collected on a Bruker D8 Advance X-ray diffractometer with Ni-filtered $\text{Cu K}\alpha$ radiation at 40 kV and 40 mA in the 2θ ranging from 10° to 80° with a scan rate of 0.02° per second. Field-emission scanning electron microscopy (FE-SEM) was used to characterize the morphology of the samples on a FEI Nova NANOSEM 230 spectrophotometer. Transmission electron microscopy (TEM), high-resolution transmission electron microscopy (HRTEM) images and elemental mapping results were obtained by a JEOL model JEM 2010 EX instrument at an acceleration voltage of 200 kV. The optical properties of the samples were analyzed by UV-vis diffuse reflectance spectroscopy (DRS) using a UV-vis spectrophotometer (Cary 500, Varian Co.), in which BaSO_4 was employed as the internal reflectance standard. The electrochemical analysis was conducted in a conventional three-electrode cell, which uses a Pt plate as the counter electrode and an Ag/AgCl electrode as the reference electrode. The working electrode was prepared on fluorine doped tin oxide (FTO) glass that was cleaned by sonication in ethanol and dried at 353 K for 2 h. The boundary of FTO glass was protected using Scotch tape. The 5 mg sample was fully dispersed in 0.5 ml of DMF by sonication to get slurry. The slurry was spread onto the pre-treated FTO glass. After air drying, the working electrode was further dried at 393 K for 2 h to improve adhesion. Then, the Scotch tape was unstuck, and the uncoated part of the electrode was isolated with epoxy resin. The exposed area of the working electrode was 0.25 cm². The photocurrent measurement was taken on a BAS Epsilon workstation with bias of 0.5 V under UV-vis light irradiation and the electrolyte was 0.2 M aqueous Na_2SO_4 solution (pH = 6.8) without additive. The electrochemical impedance spectroscopy (EIS) measurement was measured via an EIS spectrometer (CHI-660D workstation, CH Instrument) in the three-electrode cell in the presence of 0.5 M KCl solution containing 5.0 mM $\text{K}_3[\text{Fe}(\text{CN})_6]/\text{K}_4[\text{Fe}(\text{CN})_6]$ by applying an AC voltage with 5 mV amplitude in a frequency range from 1 Hz to 100 kHz under open circuit potential conditions. The Mott-Schottky experiments were obtained on CHI-660D workstation with the potential ranged from -1 V to 1 V (vs. Ag/AgCl) under three different frequencies of 0.3k Hz, 0.5k Hz, and 1k Hz and the electrolyte was 0.2 M aqueous Na_2SO_4 solution (pH = 6.8) without additive. The photoluminescence spectra (PL) for powder samples were analyzed on an Edinburgh Analytical Instrument

F900 spectrophotometer with an excitation wavelength of 340 nm. To ensure the comparability of the PL spectra, the experimental parameters, including the excitation wavelength, slit width, and the amount of the samples, were identical.

2.6. Catalyst activity

The photocatalytic reduction of CO₂ was performed in a gas-solid heterogeneous reaction mode in a quartz reactor (volume, ~25 ml). The loading mass of the photocatalyst sample was 20 mg. This system was evacuated by a mechanical pump and filled with pure CO₂ gas. The evacuation-filling operation was repeated five times. 0.5 ml of evacuated water was introduced finally with a syringe via the septum into the sample cell (5 ml) hanging in the quartz reactor. The reactor was kept in dark for 1 h to establish the adsorption-desorption equilibrium before the irradiation. A 300 W Xe arc lamp (PLS-SXE 300C, Beijing Perfect light Co., Ltd.), emitting UV-vis light (320 nm < λ < 780 nm) with an energy output of 0.8 W cm⁻² measured by a Thorlabs PM100 optical power and energy meter, was placed at a distance of approximate 5 cm from the reactor to be the irradiation source to trigger the photocatalytic reaction. The temperature of the reactor was kept at 298 K with an electronic fan. At certain irradiation time interval during the experiment, 1 ml of reactive gas was taken from the reactor with a syringe for analysis. The amounts of the products were analyzed by gas chromatography (GC 2014C) fitted with a high-sensitivity thermal conductivity detector (TCD) detector for quantifying the amounts of H₂ formed from H₂O photoreduction and a flame ionization detector (FID) detector for quantifying the amounts of CO and CH₄ formed from CO₂ photoreduction. After the effluents were separated by the PN pre-column and 5 Å molecular sieve column, H₂ and O₂ were analyzed by the TCD detector. CH₄ was analyzed by the FID detector. CO was further converted to CH₄ by a methanation reactor and then analyzed by the FID detector. The detection limits of our analytic method for CH₄ and CO were both 0.002 μmol. The detection limits for H₂ was 0.004 μmol. Argon was used as the carrier gas. The contrast activity tests were conducted by replacing CO₂ with N₂ under other reaction conditions identical.

3. Results and discussion

Fig. 1a schematically displays the flowchart for the fabrication of Bi₂WO₆-TiO₂ binanosheets (B-T). Firstly, the hydrothermally prepared TiO₂ nanosheets (TNS) were functionalized by 3-aminopropyl-triethoxysilane (APTES) to be positively charged (A-TNS); while Bi₂WO₆ nanosheets (BWO) were born to be negatively charged due to the introduction of Br⁻ ions to BWO layer surfaces during the hydrothermal process (**Fig. 1b**) [44]. The electrostatic interaction force between A-TNS (+ 39 mV of Zeta potential) and BWO (-20 mV of Zeta potential) then allows the fabrication of B-T composite through an electrostatic self-assembly approach. Field-emission scanning electron microscopy (SEM) and transmission electron microscopy (TEM) were employed to examine the morphology information and microscopic structures of the samples. **Fig. 1c** and d show the SEM and TEM images of bare TNS, respectively, both of which display the well-defined two-dimensional (2D) sheet structures of TNS. In the high-resolution TEM (HRTEM) image in the inset of **Fig. 1d**, the lattice spacing determined as 0.352 nm belongs to the (101) plane of TNS [42]. The SEM and TEM images in **Fig. 1e** and f demonstrate the sheet-shaped structures of BWO, and the marked interplanar spacing of 0.273 nm in the HRTEM image (inset of **Fig. 1f**) corresponds to (200) plane of BWO [35,44]. **Fig. 1g** discloses the TEM image of B-T composite, manifesting the compact interfacial contact between TNS and BWO. From the HRTEM image in **Fig. 1h**, both the marked interplanar spacing of 0.375 nm corresponding to (111) plane of BWO [45], and that of 0.189 nm corresponding to (200) plane of TNS can be clearly distinguished [46]. The results illustrate the successful incorporation of BWO into TNS, and the good interfacial

interaction formed between them.

X-ray diffraction (XRD) was employed to investigate the crystal phase structure of the samples. **Fig. 2a** depicts the XRD patterns of TNS, BWO and B-T composite. It is clear to see that all the diffraction peaks of pure TNS are ascribed to the anatase phase of TiO₂ (JCPDS No. 21-1272) and those of BWO are attributed to the orthorhombic Bi₂WO₆ phase (JCPDS No. 73-2020). As for B-T, both the typical diffraction peaks of TNS and BWO can be observed in the composite. **Fig. 2b** shows the UV-vis diffuse reflectance spectroscopy (DRS) data, which directly reflects the optical property of the samples. The absorption edge of bare TNS located at around 400 nm corresponds to the intrinsic absorption of anatase TiO₂ [47]. BWO shows a absorption edge around 450 nm, correlating with the intrinsic bandgap absorption of Bi₂WO₆ [44]. Compared with pure TNS, the B-T composite exhibits a slightly red-shifted absorption threshold around 420 nm, which can be assigned to the introduction of BWO [43].

In the next, we evaluated the efficiency of the sample for photocatalytic CO₂ reduction with H₂O in gas phase under UV-vis light irradiation. Considering the possible carbonaceous residues on the photocatalyst, which may decompose into small molecules such as CO and CH₄ during photocatalysis, causing overestimation of the catalytic activity [18–21], a contrast test in N₂ atmosphere instead of CO₂ under otherwise identical conditions was simultaneously conducted to confirm whether the possible carbonaceous residues contribute to the carbon-containing products formation. As shown in **Fig. 2c**, we can see that large amount of CO and CH₄ were produced from the reaction system under N₂, which should be released from the carbonaceous residues within the sample; however, once N₂ was replaced with CO₂, the detected amount of CO/CH₄ is significantly decreased, where it seems that not only photocatalytic CO₂ reduction has not efficiently proceeded but also the carbonaceous residues decomposition has been largely inhibited. Clearly, the results imply a competitive relationship between the light-driven carbonaceous residues decomposition and CO₂ photocatalytic reduction. In this regard, we propose that as for studies on photocatalytic CO₂ reduction, the recommended contrast test of activity in N₂ atmosphere instead of CO₂, aiming to exclude the participation of catalyst associated carbonaceous residues in the formation of products, might sometimes lead to underestimation of the true activity. It is because that carbonaceous residues decomposition under N₂ atmosphere might be inhibited under CO₂ atmosphere, as reflected in the case study of the as-prepared B-T sample.

The CO and CH₄ produced under N₂ atmosphere should stem from the carbonaceous residues remaining within the B-T sample, which were introduced during the synthetic process and hardly cleared up through conventional washing procedures [18,21]. In order to track out the origin of the carbonaceous residues, we have monitored the behavior of each single component of the B-T composite, including bare BWO, bare TNS, and APTES modified TNS (A-TNS), under N₂ atmosphere and UV-vis light irradiation. As shown in **Fig. 2d**, only a little amount of CO/CH₄ was detected over bare BWO and TNS. By contrast, as much as 40 μmol g⁻¹ of CO with a small amount of CH₄ was obtained within only 1 h light irradiation over A-TNS, and further increasement can be observed when lengthening the reaction time to 2 h. The results indicate that it is the process of modifying TNS with APTES that results in abundant carbonaceous residues within the final A-TNS and B-T samples, which then decompose into CO/CH₄ under UV-vis light irradiation and N₂ atmosphere.

The products yields over TNS and A-TNS in the CO₂ atmosphere have also been analyzed and summarized in **Table 1**. The comparation study between A-TNS in the CO₂ and N₂ atmosphere further confirms that CO₂ can suppress the decomposition of carbonaceous residues. As for TNS, the suppression is not obvious, which is because that only small amount of carbonaceous residues exist over TNS and the intrinsic decomposition is slight. Therefore, we can conclude that the carbonaceous residues decomposition can be greatly suppressed under CO₂ atmosphere when large amount of carbonaceous residues exist in the

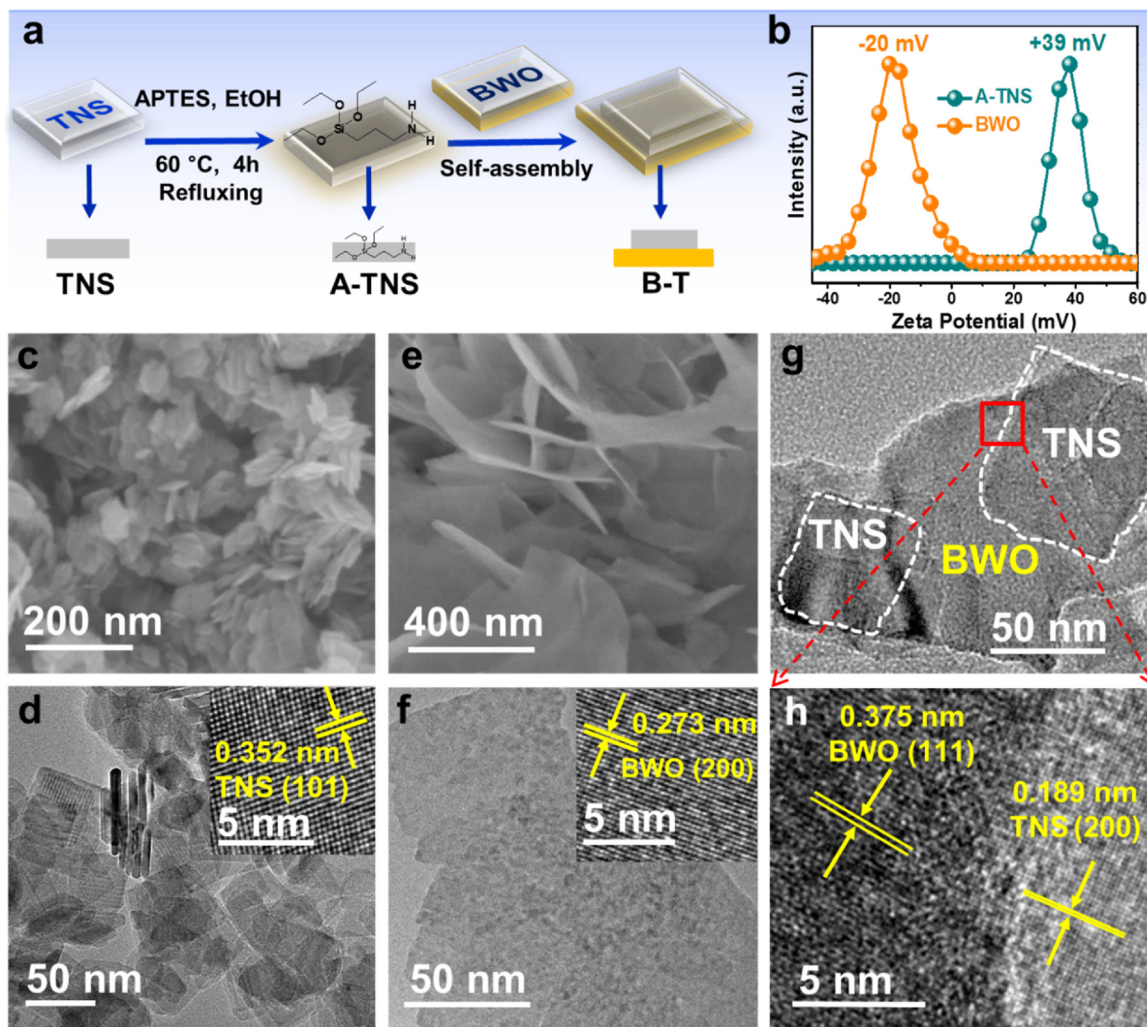


Fig. 1. Flowchart for the fabrication of A-TNS and B-T (a); Zeta potentials for A-TNS and BWO (b); SEM and TEM images for TNS (c, d) and BWO (e, f), respectively; insets of (d) and (f) are the HRTEM images of TNS and BWO, respectively; TEM and HRTEM images for B-T composite (g, h).

samples. On the other hand, the products yields comparation between TNS and A-TNS under CO₂ atmosphere indicate that since the intrinsic photoactivity of TNS for CO₂ reduction is low, the existence of the carbonaceous residues on the TNS sample disturbs the real activity measurement for CO₂ photocatalytic reduction, and the degree of the influence highly depends on the amount of the carbonaceous residues. We believe that if the photocatalyst exhibits high efficiency and good stability for CO₂ reduction, the influence of carbonaceous residues decomposition on the activity test will be negligible since the carbonaceous residues will become less and less due to the decompositon (as reflected in Fig. 3) while the true activity from CO₂ reduction is consistent. Therefore, it is vital to devote more efforts to further improve the intrinsic activity of the photocatalysts for CO₂ reduction.

More intriguing phenomenon is that under N₂ atmosphere, the obtained amount of CH₄ over B-T continually increases with the reaction time, which gradually exceeds the released amount of CO (Fig. 3a); while the products over A-TNS is mainly occupied by CO, although detectable increasement of CH₄ can also be observed (Fig. 3b). It can be concluded that the addition of BWO into A-TNS changed the products distribution by accelerating further transformation of CO to CH₄. Controlled experiments have been conducted for in-depth investigation of the undergoing reactions. Fig. 3c displays the light-driven behavior of B-T under N₂ atmosphere and UV-vis light irradiation, but without the addition of H₂O. It can be found that further transformation of CO to CH₄ was failed to happen without H₂O, which is in accordance with

the reaction mechanism of photocatalytic CO₂ reduction. That is, H₂O is indispensable in the reduction of CO₂/CO to CH₄, which plays the role of to be oxidized to provide proton H⁺ to participate in the reaction [12,13,18]. Obviously, the results show an integrative relationship between light-driven carbonaceous residues decomposition and CO₂ photocatalytic reduction. Specifically, the released CO from the carbonaceous residues decomposition can be further reduced to CH₄, which is one of the key reaction steps in photocatalytic CO₂ reduction [12,13,18]. Fig. 3d shows the products distribution of the sample consisted of physically mixed A-TNS and BWO (denoted as A-TNS + BWO). We can see that CO is the major product with negligible CH₄ formation, which suggests that the compact interfacial contact between TNS and BWO, the critical factor to interfacial charge transfer, plays an important role in boosting further reduction of CO to CH₄. The slight difference of the CO yield between the samples of A-TNS and A-TNS + BWO is because that the addition of the BWO component possibly changed the adsorbing behavior of the samples over the intermediate and/or final products during the reaction process, since it has been reported that the high oxygen affinity of Bi enables strong adsorption of CO on the Bi surface [48,49]. The above results suggest that, as compared to A-TNS, the enhanced H₂O oxidation was obtained over B-T composite and subsequently more proton H⁺ was achieved to result in enhanced transformation of CO to CH₄. In addition, a trace amount of H₂ was also detected over the B-T sample after 8 h light irradiation under N₂ atmosphere (Table 1), which is because that the accumulated

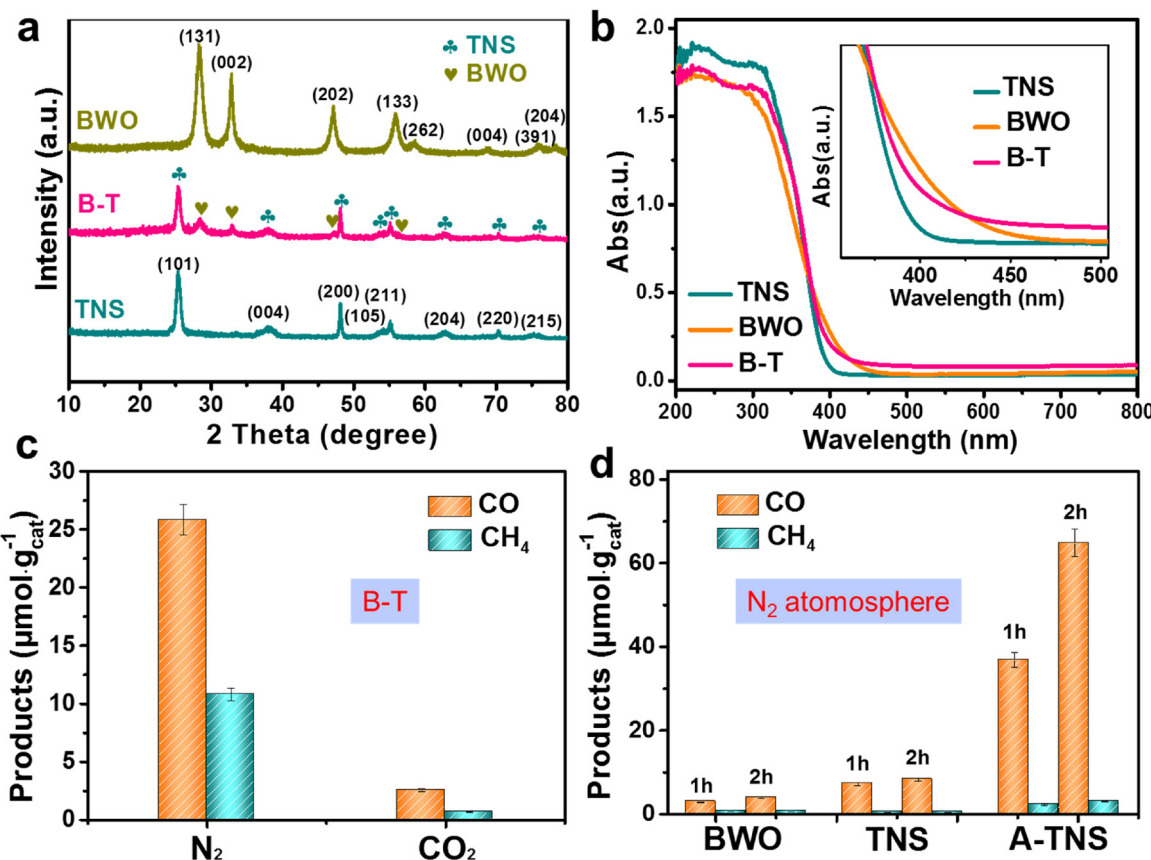


Fig. 2. XRD patterns of TNS, BWO, and B-T composite (a); DRS of TNS, BWO and B-T, inset is the enlarged DRS ranges from 320 to 510 nm (b); the products distribution after 1 h light irradiation over B-T composite under N_2 and CO_2 atmosphere, respectively (c); products distribution over BWO, TNS and A-TNS under N_2 atmosphere within 2 h light irradiation (d). Reaction conditions: 20 mg of catalysts, 0.5 ml of water, under UV-vis light irradiation. Note that the error bars represent the photoactivity standard deviation values calculated from triplicate experiments.

Table 1

Yields of H_2 , CH_4 and CO as a result of the photoreaction over different samples under N_2 or CO_2 atmosphere. Reaction conditions: 20 mg of catalysts, 0.5 ml of water, and UV-vis light irradiation.

Samples	reaction atmosphere	reaction time(h)	H_2 ($\mu\text{mol g}^{-1}$)	CH_4 ($\mu\text{mol g}^{-1}$)	CO ($\mu\text{mol g}^{-1}$)
B-T	N_2	1	n.d.	10.8	25.8
	CO_2	1	n.d.	0.7	2.6
TNS	N_2	2	n.d.	0.5	8.3
	CO_2	2	n.d.	1.6	6.9
A-TNS	N_2	2	n.d.	3.1	64.8
	CO_2	2	n.d.	1.5	24.3
BWO	N_2	2	n.d.	0.6	2.9
B-T	N_2	8	trace	48.6	43.7
A-TNS	N_2	8	n.d.	11.7	101.4
B-T	N_2 without H_2O	8	n.d.	3.0	50.6
ATNS + BWO	N_2	8	n.d.	3.4	92.5

Note: n.d. = not detected.

proton H^+ also leads to the formation of H_2 , an important competitive reaction with the reduction of CO_2 during photocatalytic CO_2 reduction with H_2O [3,12].

In order to figure out the mechanisms for the higher H_2O oxidation efficiency over B-T than bare TNS, the relative band positions of BWO and TNS are firstly identified. According to the Mott-Schottky results (Fig. 4a and b), the flat-band potential of TNS and BWO are estimated to be around -0.9 V and -0.23 V versus Ag/AgCl ($\text{pH} = 6.8$, for 0.2 M Na_2SO_4 electrolyte), respectively [50,51]. Since both BWO and TNS show the characteristic behavior of n-type semiconductor, as observed from the positive slope of the linear plots [51], their conduction band

edges (CB) are considered to be very close to their flat-band potentials [51]. Therefore, the CB of TNS and BWO are calculated to be -0.28 V and $+0.39$ V vs. normal hydrogen electrode (NHE, $\text{pH} = 0$), respectively. According to the Kubelka-Munk function based on the DRS spectra (Fig. 2b), the bandgap energy of TNS and BWO are calculated to be ≈ 3.2 eV and ≈ 2.7 eV, respectively, from the intercept of the tangents to the plots of $[ahv]^{1/2}$ versus photon energy ($h\nu$), since both TiO_2 and Bi_2WO_6 are indirect bandgap semiconductors (Fig. 4c) [24,44]. The valence band (VB) of TNS and BWO are then determined as $+2.92$ V and $+3.09$ V using the formula $E_{\text{CB}} = E_{\text{VB}} - E_g$. Based on the matchable energy band between TNS and BWO, two possible charge transfer routes are proposed: conventional type II and direct Z-scheme heterojunction mechanisms. If the B-T composite follow the conventional type II charge transfer mechanism (Fig. 4d), under UV-vis irradiation, the photogenerated holes would tend to transfer from the VB of BWO to the VB of TNS, while the electrons from the CB of TNS to the CB of BWO, through which the oxidation ability of holes would be reduced [52]. It is clearly not consistent with the experimental results of enhanced H_2O oxidation. Therefore, it is considered that B-T composite should follow the Z-scheme charge transfer mechanism [17,43]. As shown in Fig. 4e, the combination of electrons from the CB of BWO and the holes from the VB of TNS leads to more effective holes on the VB of BWO for the oxidation of H_2O , which provides more proton H^+ to produce CH_4 [53,54].

The enhanced charge carrier transfer through Z-scheme mechanism within B-T as compared to bare BWO and TNS was further confirmed by photoelectrochemistry and photoluminescence (PL) characterizations. As shown in Fig. 4f, significantly improved photocurrent values can be observed over B-T as compared to bare BWO and TNS, demonstrating

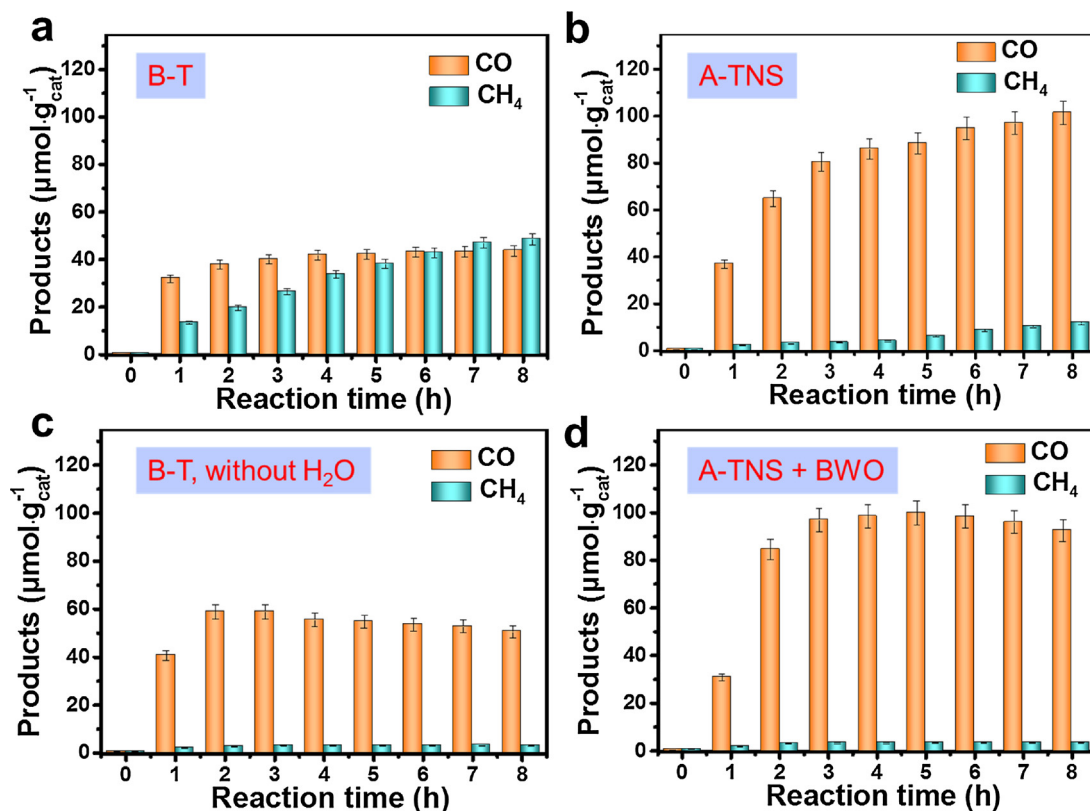


Fig. 3. The products distribution over B-T composite (a), A-TNS (b), B-T composite without H₂O addition to the reaction system (c), and physically mixed A-TNS and BWO (d) during 8 h light irradiation. Reaction conditions: 20 mg of catalysts, 0.5 ml of water, under N₂ atmosphere, and UV-vis light irradiation. Note that the error bars represent the photoactivity standard deviation values calculated from triplicate experiments.

the more efficient charge transfer achieved within B-T composite [34]. The electrochemical impedance spectroscopy (EIS) Nyquist plots were measured to gain insight into the charge transfer process on the sample electrodes as well as the contact interface between electrode and electrolyte [55]. As displayed in Fig. 4g, the Nyquist diagrams of B-T electrodes show depressed semicircle as compared to bare BWO and TNS, indicating that the introduction of BWO contributes to enhanced charge transfer. The photoluminescence (PL) spectrum of the samples conducted under 340 nm monochromatic light excitation was employed to study the recombination of electron-hole pairs. As shown in Fig. 4h, the PL profile of B-T is similar to that of TNS and obviously different from bare BWO. This is because of the relatively low amount of BWO in the B-T composite, and it is reasonable to conclude that the PL emission peak for B-T is mainly attributed to that of TNS [56]. Notably, the PL intensity of B-T is much lower than that of pure TNS, suggesting the more efficient inhibition of radiative recombination of electron-hole pairs in the B-T composite [57]. As a result, the enhanced charge transfer in the Z-scheme manner within B-T composite leads to enhanced H₂O oxidation and subsequently more proton H⁺, which ultimately further transforms CO as the major product for A-TNS to CH₄, as schematically illustrated in Fig. 4i. These results provide some enlightenment on designing more efficient photocatalysts for CO₂ reduction, where the rationally designed Z-scheme based composites without the disturbance of carbonaceous residues would be of great potential for achieving high selectivity for CH₄ formation.

4. Conclusion

Bi₂WO₆-TiO₂ (B-T) binanosheets have been prepared through an electrostatic self-assembly between positively charged A-TNS and negatively charged BWO, based on which we have unveiled the interplay, i.e., the co-existence of a competition and an interaction between light-

driven CO₂ photocatalytic reduction and carbonaceous residues decomposition, as schematically shown in Fig. 4i. Although the true activity of as-fabricated B-T for photocatalytic CO₂ reduction is hard to be confirmed, some enlightenment on the future researches in the field of gas-phase photocatalytic CO₂ reduction are highlighted. Firstly, the photoactive materials is better to be synthesized avoiding introduction of large amounts of carbon containing reagents, such as surfactant or polymer, which could complicate accurate evaluation of the true photoactivity; and/or post-treatment such as UV-irradiation or thermal activation in air can be employed to remove possible residues on the condition of not destroying the structure and properties of the materials. Secondly, the contrast test of activity under inert gas instead of CO₂ to exclude the contribution of carbonaceous residues to the products formation might lead to underestimation of the true activity, since CO₂ molecules could play a role in suppressing the carbonaceous residues decomposition. At last, the enhanced Z-scheme charge transfer between BWO and TNS can reduce more CO released from the carbonaceous residues to CH₄, and thus it is reasonable to propose that more rationally designed Z-scheme based composites without the disturbance of carbonaceous residues would be a promising material to obtain higher selectivity for CH₄ formation in photocatalytic CO₂ reduction.

Acknowledgements

The support from the National Natural Science Foundation of China (NSFC) (U1463204, 21173045), the Award Program for Minjiang Scholar Professorship, the Natural Science Foundation (NSF) of Fujian Province for Distinguished Young Investigator Rolling Grant (2017J07002), the Independent Research Project of State Key Laboratory of Photocatalysis on Energy and Environment (NO. 2014A05), and the 1st Program of Fujian Province for Top Creative Young Talents is gratefully acknowledged.

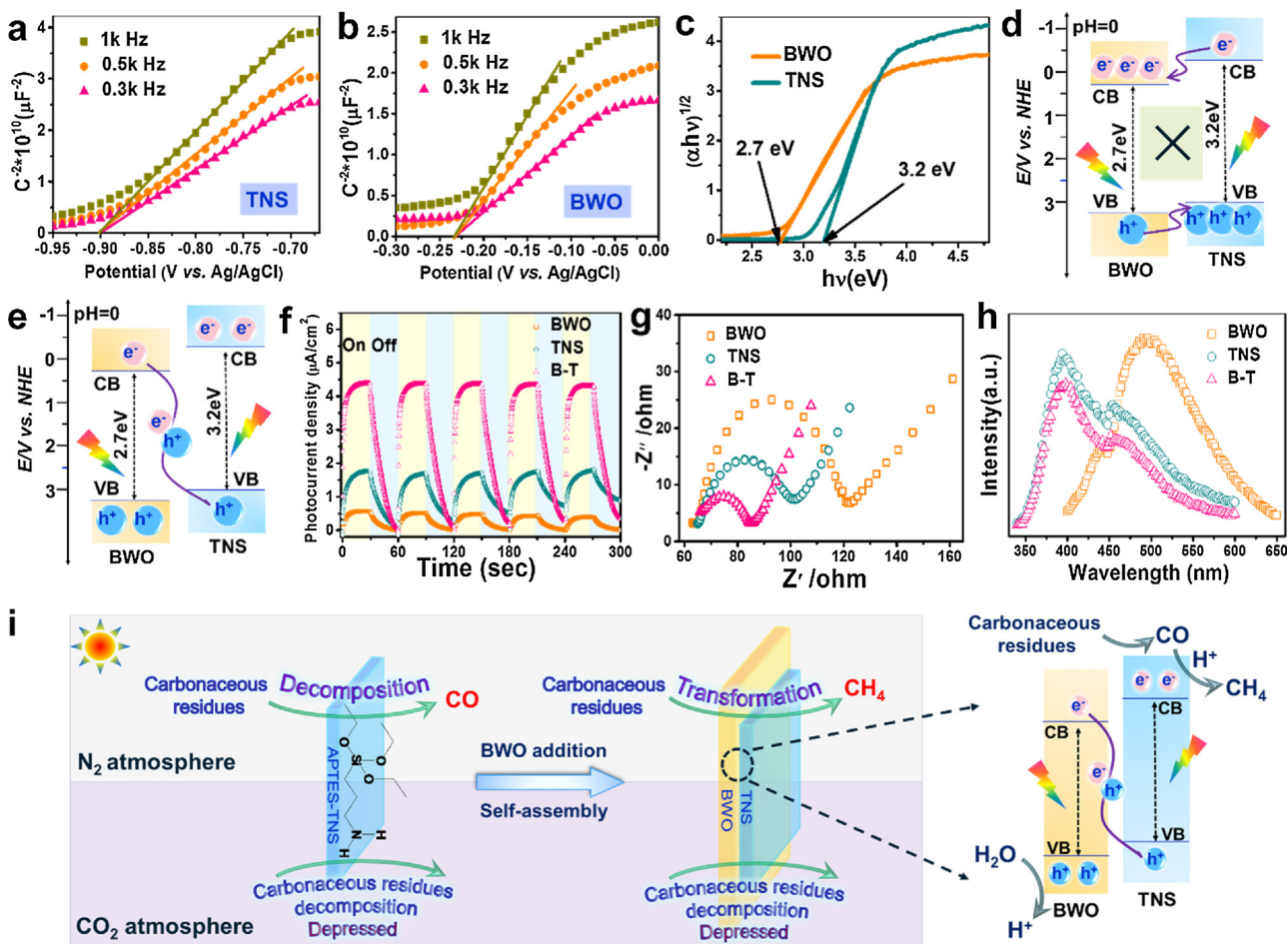


Fig. 4. Mott-Schottky plots for TNS (a) and BWO (b); the estimated energy bandgap by the plot based on the Kubelka-Munk function *versus* the energy of light for TNS and BWO based on the DRS spectra in Fig. 2b (c); schematic illustrating the relative energy band levels of TNS and BWO, and the possible charge transfer mechanism between them: type II charge transfer (d), and Z-scheme charge transfer (e); photocurrent density under UV-vis light irradiation (f), EIS Nyquist plots (g), and PL emission spectra with an excitation wavelength of 340 nm (h) for the samples of bare BWO, bare TNS and B-T composite; schematic diagram of the reaction process (i).

References

- [1] A. Nikokavoura, C. Trapalis, *Appl. Surf. Sci.* 391 (2017) 149–174.
- [2] Y. Zheng, W. Zhang, Y. Li, J. Chen, B. Yu, J. Wang, L. Zhang, J. Zhang, *Nano Energy* 40 (2017) 512–539.
- [3] W. Tu, Y. Zhou, Z. Zou, *Adv. Mater.* 26 (2014) 4607–4626.
- [4] S. Xie, Q. Zhang, G. Liu, Y. Wang, *Chem. Commun.* 52 (2016) 35–59.
- [5] K. Li, X. An, K.H. Park, M. Khrasheh, J. Tang, *Catal. Today* 224 (2014) 3–12.
- [6] C. Song, *Catal. Today* 115 (2006) 2–32.
- [7] J. Su, L. Vayssières, *ACS Energy Lett.* 1 (2016) 121–135.
- [8] H. Zhou, X. Li, T. Fan, F.E. Osterloh, J. Ding, E.M. Sabio, D. Zhang, Q. Guo, *Adv. Mater.* 22 (2010) 951–956.
- [9] D. Kim, K.K. Sakimoto, D. Hong, P. Yang, *Angew. Chem. Int. Ed.* 54 (2015) 3259–3266.
- [10] L. Yuan, Y.-J. Xu, *Appl. Surf. Sci.* 342 (2015) 154–167.
- [11] W. Tu, Y. Zhou, Z. Zou, *Adv. Funct. Mater.* 23 (2013) 4996–5008.
- [12] S.N. Habreutinger, L. Schmidt-Mende, J.K. Stolarczyk, *Angew. Chem. Int. Ed.* 52 (2013) 7372–7408.
- [13] X. Chang, T. Wang, J. Gong, *Energy Environ. Sci.* 9 (2016) 2177–2196.
- [14] A. Corma, H. Garcia, *J. Catal.* 308 (2013) 168–175.
- [15] J. Low, J. Yu, W. Ho, *J. Phys. Chem. Lett.* 6 (2015) 4244–4251.
- [16] M.-Q. Yang, Y.-J. Xu, *Nanoscale Horiz.* 1 (2016) 185–200.
- [17] P. Zhou, J. Yu, M. Jaroniec, *Adv. Mater.* 26 (2014) 4920–4935.
- [18] K. Li, B. Peng, T. Peng, *ACS Catal.* 6 (2016) 7485–7527.
- [19] J. Wu, Y. Huang, W. Ye, Y. Li, *Adv. Sci.* 4 (2017) 1700194.
- [20] I. Grigioni, M.V. Dozzi, M. Bernareggi, G.L. Chiarello, E. Selli, *Catal. Today* 281 (2017) 214–220.
- [21] C.-C. Yang, Y.-H. Yu, B. van der Linden, J.C.S. Wu, G. Mul, *J. Am. Chem. Soc.* 132 (2010) 8398–8406.
- [22] Y. Ma, X. Wang, Y. Jia, X. Chen, H. Han, C. Li, *Chem. Rev.* 114 (2014) 9987–10043.
- [23] V.P. Indrakanti, J.D. Kubicki, H.H. Schobert, *Energy Environ. Sci.* 2 (2009) 745–758.
- [24] N. Sakai, Y. Ebina, K. Takada, T. Sasaki, *J. Am. Chem. Soc.* 126 (2004) 5851–5858.
- [25] K. Mori, H. Yamashita, M. Anpo, *RSC Adv.* 2 (2012) 3165–3172.
- [26] Z. Xiong, Z. Lei, C.-C. Kuang, X. Chen, B. Gong, Y. Zhao, J. Zhang, C. Zheng, J.C.S. Wu, *Appl. Catal. B: Environ.* 202 (2017) 695–703.
- [27] Z. Xiong, Y. Luo, Y. Zhao, J. Zhang, C. Zheng, J.C.S. Wu, *Phys. Chem. Chem. Phys.* 18 (2016) 13186–13195.
- [28] L. Liu, Y. Jiang, H. Zhao, J. Chen, J. Cheng, K. Yang, Y. Li, *ACS Catal.* 6 (2016) 1097–1108.
- [29] S. Xie, Y. Wang, Q. Zhang, W. Deng, Y. Wang, *ACS Catal.* 4 (2014) 3644–3653.
- [30] Q. Zhai, S. Xie, W. Fan, Q. Zhang, Y. Wang, W. Deng, *Angew. Chem. Int. Ed.* 52 (2013) 5776–5779.
- [31] L. Liu, C. Zhao, H. Zhao, D. Pitts, Y. Li, *Chem. Commun.* 49 (2013) 3664–3666.
- [32] S. Xie, Y. Wang, Q. Zhang, W. Fan, W. Deng, Y. Wang, *Chem. Commun.* 49 (2013) 2451–2453.
- [33] R. Long, Y. Li, Y. Liu, S. Chen, X. Zheng, C. Gao, C. He, N. Chen, Z. Qi, L. Song, J. Jiang, J. Zhu, Y. Xiong, *J. Am. Chem. Soc.* 139 (2017) 4486–4492.
- [34] Y. Jia, S. Zhan, S. Ma, Q. Zhou, *ACS Appl. Mater. Interfaces* 8 (2016) 6841–6851.
- [35] J. Tian, Y. Sang, G. Yu, H. Jiang, X. Mu, H. Liu, *Adv. Mater.* 25 (2013) 5075–5080.
- [36] J. Xu, W. Wang, S. Sun, L. Wang, *Appl. Catal. B: Environ.* 111–112 (2012) 126–132.
- [37] G. Colon, S. Murcia Lopez, M.C. Hidalgo, J.A. Navio, *Chem. Commun.* 46 (2010) 4809–4811.
- [38] Y. Lu, K. Zhao, Y. Zhao, S. Zhu, X. Yuan, M. Huo, Y. Zhang, Y. Qiu, *Colloids Surf. A: Physicochem. Eng. Asp.* 481 (2015) 252–260.
- [39] J. Zhang, L. Huang, L. Yang, Z. Liu, X. Wang, G. Xu, E. Zhang, H. Wang, Z. Kong, J. Xi, Z. Ji, *J. Alloys Compd.* 676 (2016) 37–45.
- [40] S. Murcia Lopez, M.C. Hidalgo, J.A. Navio, G. Colon, J. Hazard. Mater. 185 (2011) 1425–1434.
- [41] N. Zhang, R. Ciriminna, M. Pagliaro, Y.-J. Xu, *Chem. Soc. Rev.* 43 (2014) 5276–5287.
- [42] B. Weng, Q. Quan, Y.-J. Xu, *J. Mater. Chem. A* 4 (2016) 18366–18377.
- [43] L. Yuan, B. Weng, J.C. Colmenares, Y. Sun, Y.-J. Xu, *Small* 13 (2017) 1702253.
- [44] Y. Zhou, Y. Zhang, M. Lin, J. Long, Z. Zhang, H. Lin, J.C. Wu, X. Wang, *Nat. Commun.* 6 (2015) 8340–8347.

- [45] L. Zhang, H. Wang, Z. Chen, P.K. Wong, J. Liu, *Appl. Catal. B: Environ.* 106 (2011) 1–13.
- [46] S.-J. Bao, C.M. Li, J.-F. Zang, X.-Q. Cui, Y. Qiao, J. Guo, *Adv. Funct. Mater.* 18 (2008) 591–599.
- [47] Z. Zhang, Y. Huang, K. Liu, L. Guo, Q. Yuan, B. Dong, *Adv. Mater.* 27 (2015) 5906–5914.
- [48] L. Liu, F. Gao, H. Zhao, Y. Li, *Appl. Catal. B: Environ.* 134–135 (2013) 349–358.
- [49] S. Jeong, W.D. Kim, S. Lee, K. Lee, S. Lee, D. Lee, D.C. Lee, *ChemCatChem* 8 (2016) 1641–1645.
- [50] W. Wu, G. Liu, S. Liang, Y. Chen, L. Shen, H. Zheng, R. Yuan, Y. Hou, L. Wu, *J. Catal.* 290 (2012) 13–17.
- [51] A. Ishikawa, T. Takata, J.N. Kondo, M. Hara, H. Kobayashi, K. Domen, *J. Am. Chem. Soc.* 124 (2002) 13547–13553.
- [52] J. Low, J. Yu, M. Jaroniec, S. Wageh, A.A. Al-Ghamdi, *Adv. Mater.* 29 (2017) 1601694.
- [53] K.-L. Bae, J. Kim, C.K. Lim, K.M. Nam, H. Song, *Nat. Commun.* 8 (2017) 1156.
- [54] J. Jin, J. Yu, D. Guo, C. Cui, W. Ho, *Small* 11 (2015) 5262–5271.
- [55] M.-Q. Yang, Y.-J. Xu, W. Lu, K. Zeng, H. Zhu, Q.-H. Xu, G.W. Ho, *Nat. Commun.* 8 (2017) 14224–14232.
- [56] B. Han, S. Liu, Y.-J. Xu, Z.-R. Tang, *RSC Adv.* 5 (2015) 16476–16483.
- [57] J. Yu, T. Ma, S. Liu, *Phys. Chem. Chem. Phys.* 13 (2011) 3491–3501.